Supplementary Information

A Novel Amorphous P_4SSe_2 Material as High-Performance Anode for Sodium-ion Batteries in Ether-based Electrolyte

Jiale Yu,[a,b] Haiyan Zhang,*[a] Emilia Olsson,[b] Tianhao Yu,[b] Zhenjiang Liu,[a] Shangshang Zhang,[a] Xifeng Huang,[a] Wenwu Li,*[a] and Qiong Cai*[b]

[a] School of Materials and Energy, Guangdong University of Technology, Guangzhou 510006, China.

[b] Department of Chemical and Process Engineering, University of Surrey, Guildford, GU2 7XH, UK.

*Corresponding author Email: hyzhang@gdut.edu.cn (Haiyan Zhang), wenwuli@gdut.edu.cn (Wenwu Li), q.cai@surrey.ac.uk (Qiong Cai)

The supporting information contains an atomic representation of the P_4SSe_2 cage molecule (Figure S1), XRD patterns of crystal P_4SSe_2 and amorphous P_4SSe_2 (Figure S2), variation of P_4SSe_2 materials in various electrolytes after 3 months (Figure S3), HRTEM image of crystal P_4SSe_2 (Figure S4), low-magnitude SEM and TEM images of amorphous P_4SSe_2 (Figure S5), EDS mapping analysis of amorphous P_4SSe_2 and its corresponding EDS spectrum (Figure S6), kinetic analysis of the a-P_4SSe_2 electrode (Figure S7), *ex situ* HRTEM images and the corresponding FFT patterns of amorphous P_4SSe_2 material at different potentials as noted on images (Figure S8-S9), enlarged XRD pattern of amorphous P_4SSe_2 electrode collected at different charging/discharging states (Figure S10-S13), Raman signal of Na_3P (Figure S14), calculated HOMO and LUMO levels for various sodium salts and solvent molecules (Table S1), geometrical optimization of different solvation clusters (Figure S15-S19), comparisons of solvation energy for the EC_x-Na, DEC_x-Na, $EC_xDEC_{5-x}Na$ and $DEC_xEC_{3-x}Na$ clusters (Figure S20), SEM images of the electrode surface after cycling at 100 mA g^{-1} for 1 cycle (Figure S21), the atomic contents of various elements at different etching depth, calculated from the XPS depth profile in various electrolytes (Figure S22) and high-resolution XPS spectrums of C 1s, Na 1s and O 1s at different etching depth in in various electrolytes (Figure S23-S28).

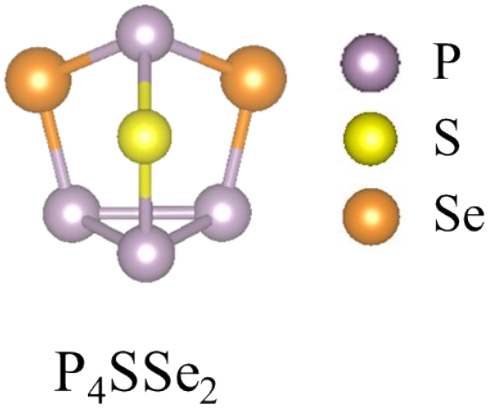

Figure S1. An example of the cage-shaped basic unit in the structure of P_4SSe_2 [1,2].

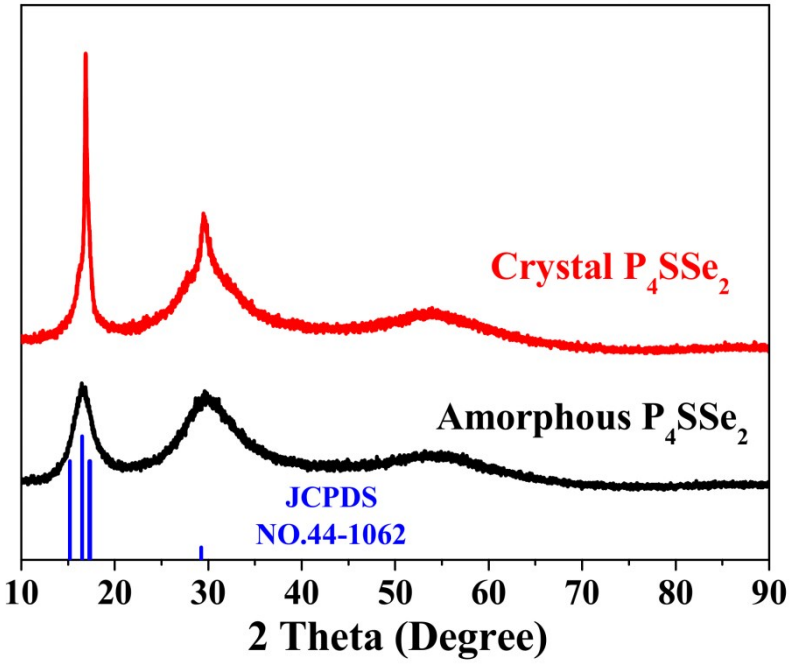

Figure S2. The XRD patterns of crystal P_4SSe_2 and amorphous P_4SSe_2.

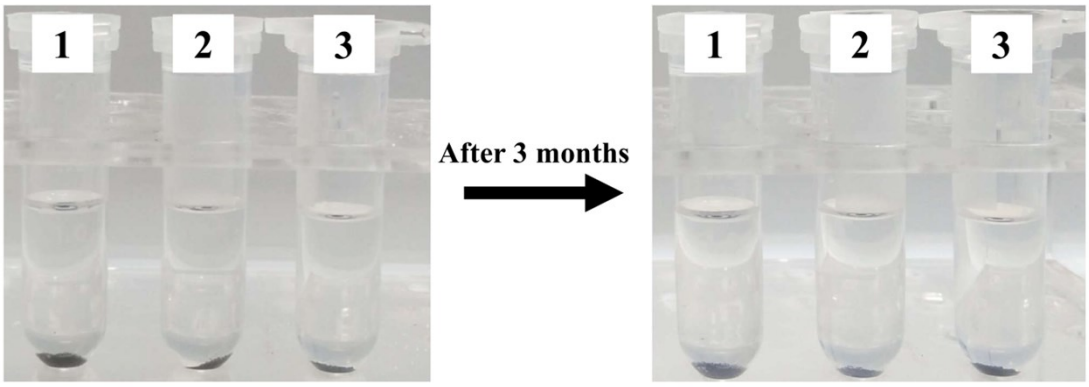

Figure S3. Desolvation of P_4SSe_2 materials with the same weight in the investigated electrolytes, where 1 is 1 M $NaCF_3SO_3$ dissolved in diglyme, 2 is 1 M $NaPF_6$ dissolved in a mixture of ethylene carbonate (EC) and diethyl carbonate (DEC) (volume ratio = 1:1), and 3 is 1 M $NaClO_4$ dissolved in a mixture of EC and DEC (volume ratio = 1:1).

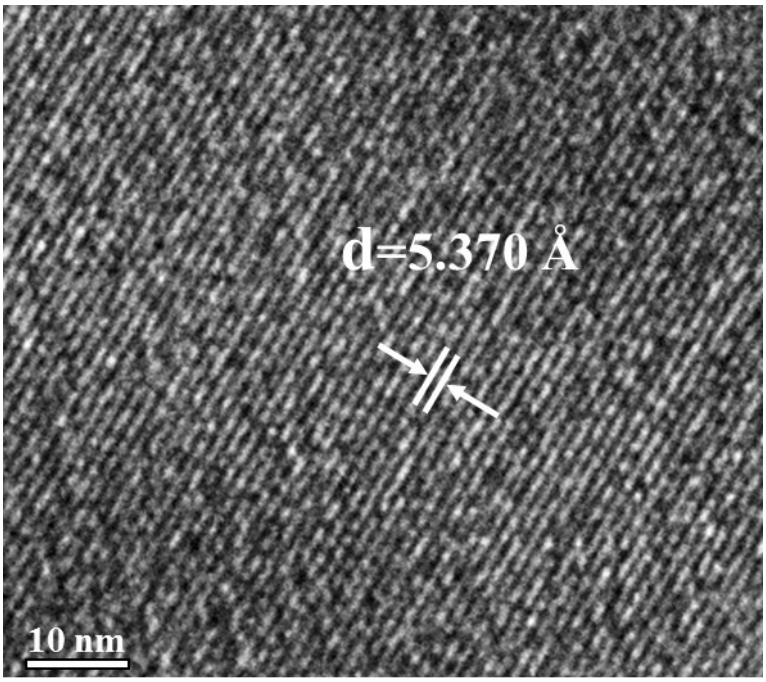

Figure S4. High–resolution transmission electron image (HRTEM) of the crystal P_4SSe_2.

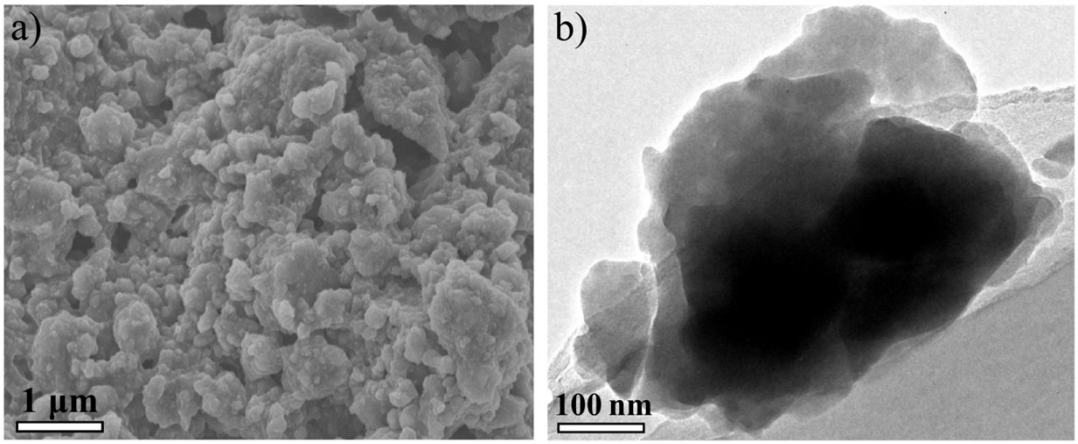

Figure S5. a) Low-magnitude field-emission scanning electron images of the amorphous P_4SSe_2 phase, and b) low-magnitude transmission electron image.

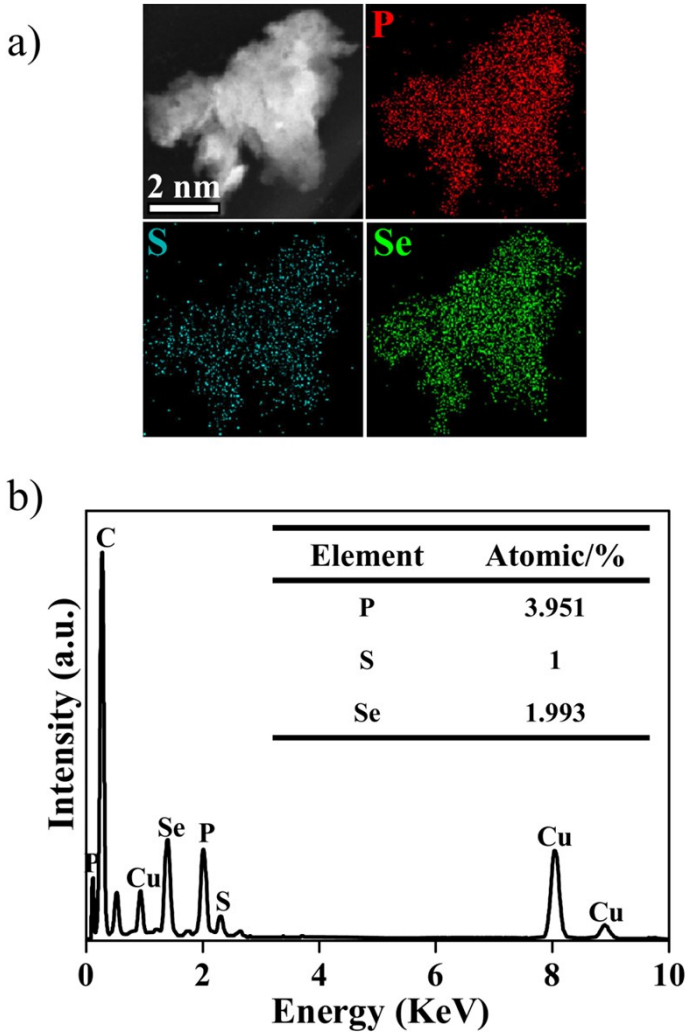

Figure S6. a) Energy-dispersive X-ray spectroscopy (EDS) mapping analysis of P_4SSe_2, and b) EDS spectrum and the inset with the P/S/Se molar ratios.

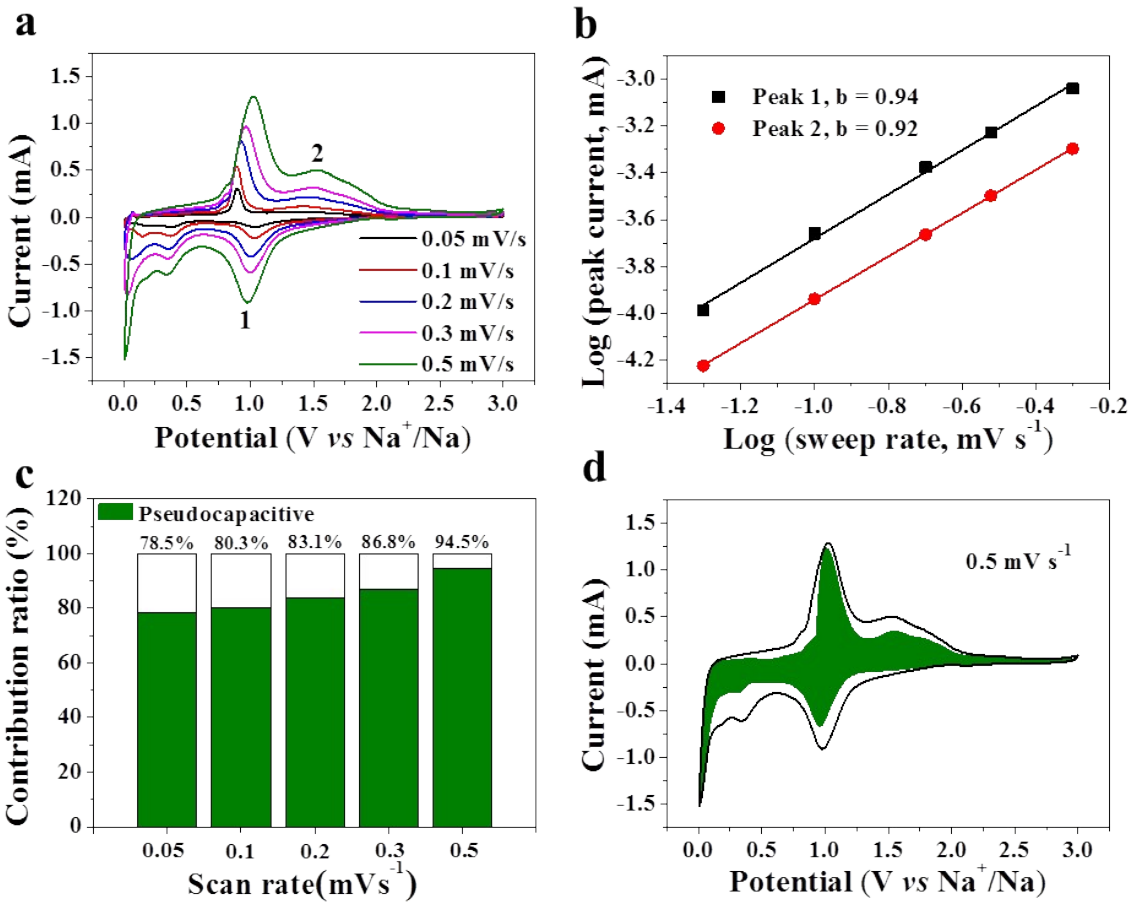

Figure S7. Kinetic analysis of a-P_4SSe_2 electrode: a) CV curves of a-P_4SSe_2 at various sweep rate, b) the relationship between log (sweep rate) and log (peak current) of a-P_4SSe_2, c) the pseudocapacitive and diffusion controlled contribution to Na storage of a-P_4SSe_2 at 0.5 mV s^{-1}, and d) the pseudocapacitive contributions of a-P_4SSe_2 at various scan rates.

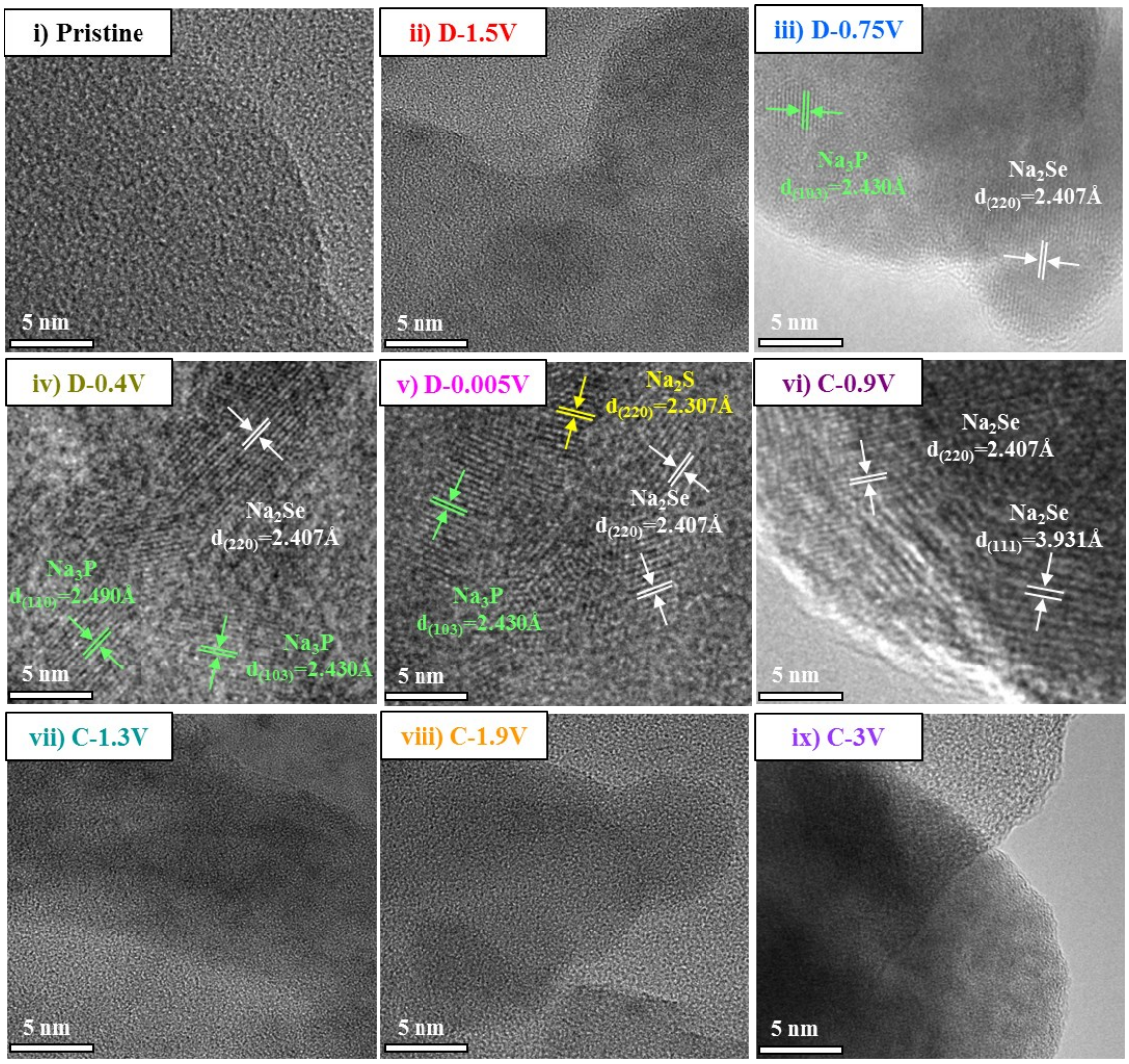

Figure S8. The *ex situ* HRTEM images of amorphous P_4SSe_2 material at different potentials as noted on images.

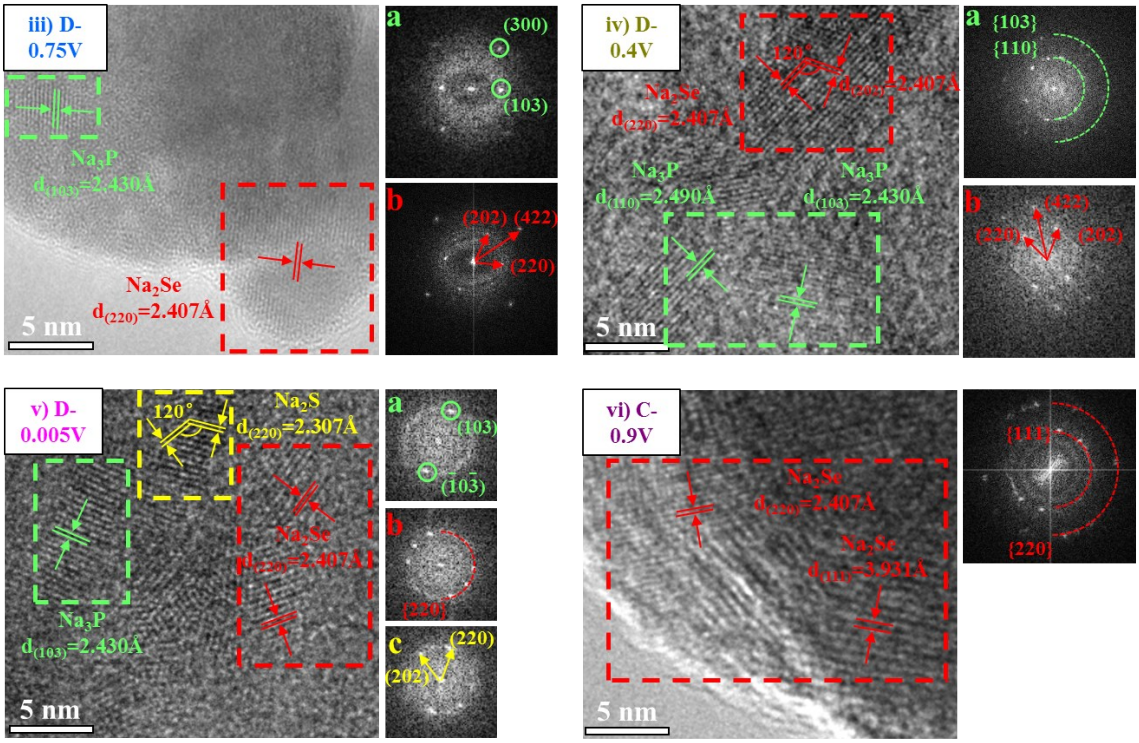

Figure S9. Fast Fourier transform (FFT) analysis of corresponding *ex situ* HRTEM images in Figure S8.

For accuracy, we further analyzed the corresponding *ex situ* HRTEM images in Fig. S8 via Fast Fourier transform (FFT). The lattice spacing of 2.430 Å is assigned to the (103) lattice planes of Na_3P and the FFT plot pattern of the selected area can be indexed to $[0\bar{1}0]$ zone axis. In addition, the Na_2Se with (220) lattice spacing of 2.407 Å also shows $[\bar{1}11]$ zone axis in its FFT image. Similarly, the lattice fringes with a spacing of 2.307 Å match well with the (220) plane of Na_2S and its FFT image also shows $[\bar{1}11]$ zone axis.

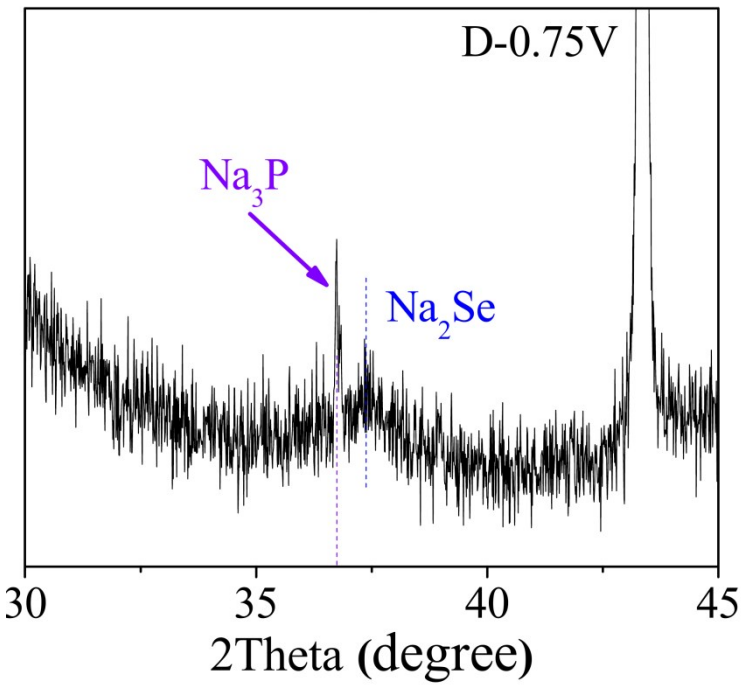

Figure S10. Enlarged XRD pattern of P_4SSe_2 electrode collected at the discharged state of 0.75 V (corresponding to Figure 3aiii in the main paper).

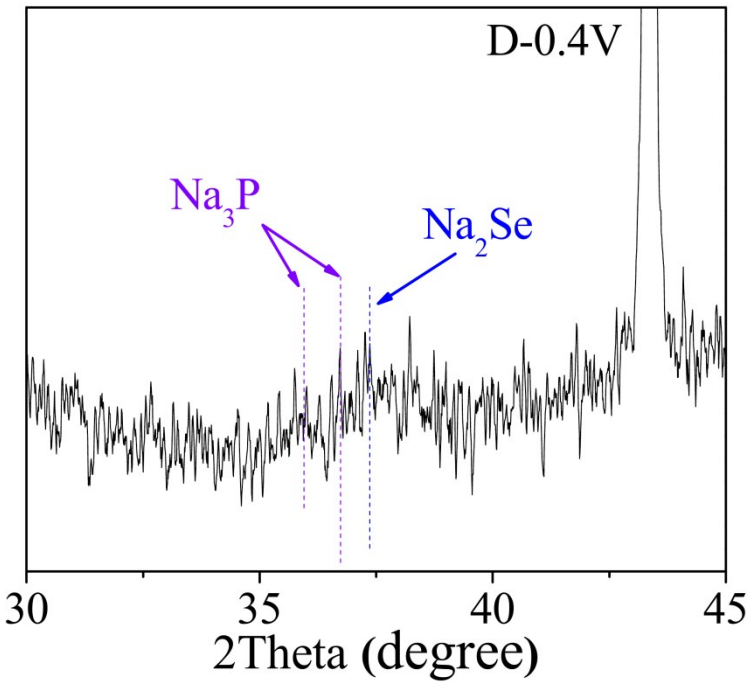

Figure S11. Enlarged XRD pattern of P_4SSe_2 electrode collected at the discharged state of 0.4 V (corresponding to Figure 3aiv in the main paper).

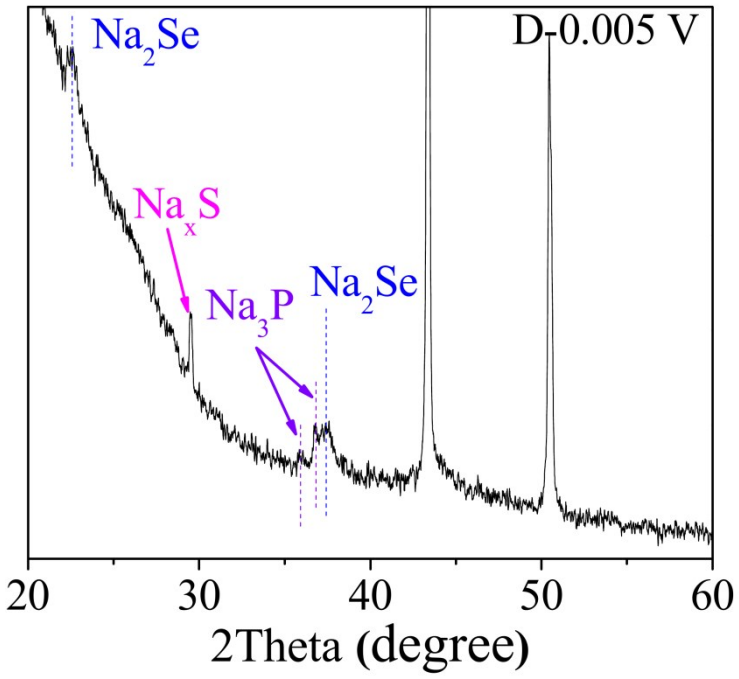

Figure S12. Enlarged XRD pattern of P_4SSe_2 electrode collected at the fully discharged state of 0.005 V (corresponding to Figure 3v in the main paper).

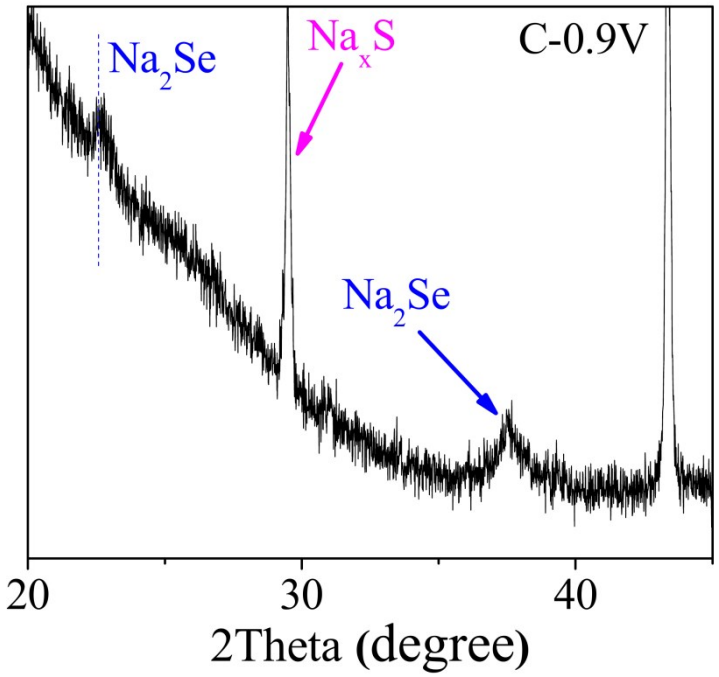

Figure S13. Enlarged XRD pattern of P_4SSe_2 electrode collected at the charged state of 0.9 V (corresponding to Figure 3avi in the main paper).

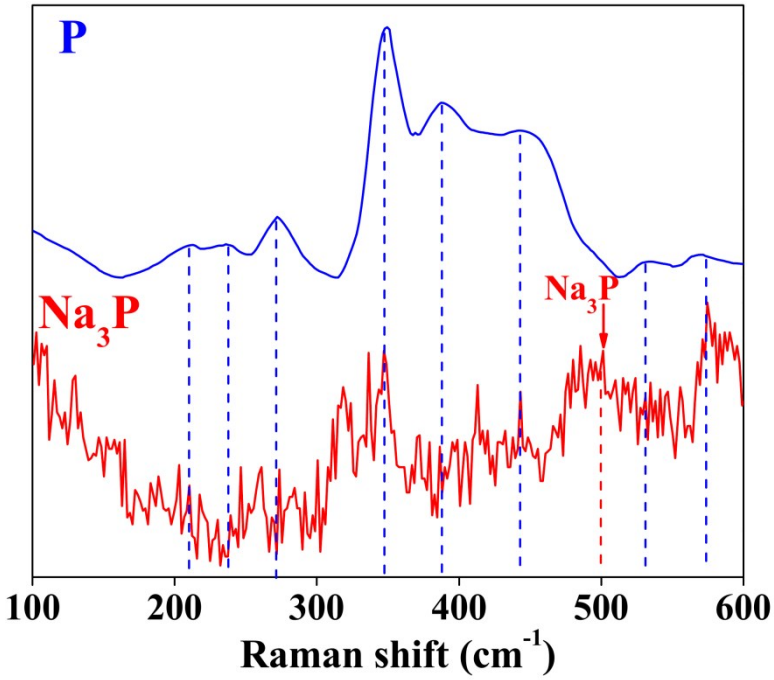

Figure S14. Raman spectrum of Na_3P sample compared with the amorphous phosphorus.

To the best of our knowledge, there is no relevant Raman spectroscopy of Na_3P in the previously reported literature. Therefore, we assembled a sodium-ion battery with the amorphous phosphorus and sodium metal as cathode and anode, respectively, to be able to compare the results presented in Fig 3b in the main paper. As shown in Figure S12, there is an extra peak located at 499.57 cm^{-1} compared with the Raman spectrum of amorphous phosphorus, which can also be constantly found in the *ex situ* Raman measurements from the discharge state of 0.75 V to the charge state of 0.5 V (Figure 3biii-vi). In addition, the signal of Na_3P can also be found at 36.04° and 36.96° in the *ex situ* XRD tests (Figure 3aiii-v). The above analysis confirms the formation of Na_3P.

Table S1. The calculated values of the highest occupied molecular orbital (HOMO) and the lowest unoccupied molecular orbital (LUMO) in diglyme and EC:DEC electrolytes. This data was obtained following the methodology outlined in Section 2.4 of the main paper [3–6].

Electrolyte	Compound	HOMO (eV)	LUMO (eV)
Diglyme	$NaCF_3SO_3$	-7.17	-0.44
	Diglyme	-6.77	2.42
EC:DEC	$NaClO_4$	-7.76	-0.27
	$NaPF_6$	-9.66	-0.17
	DEC	-7.89	1.01
	EC	-8.16	0.83

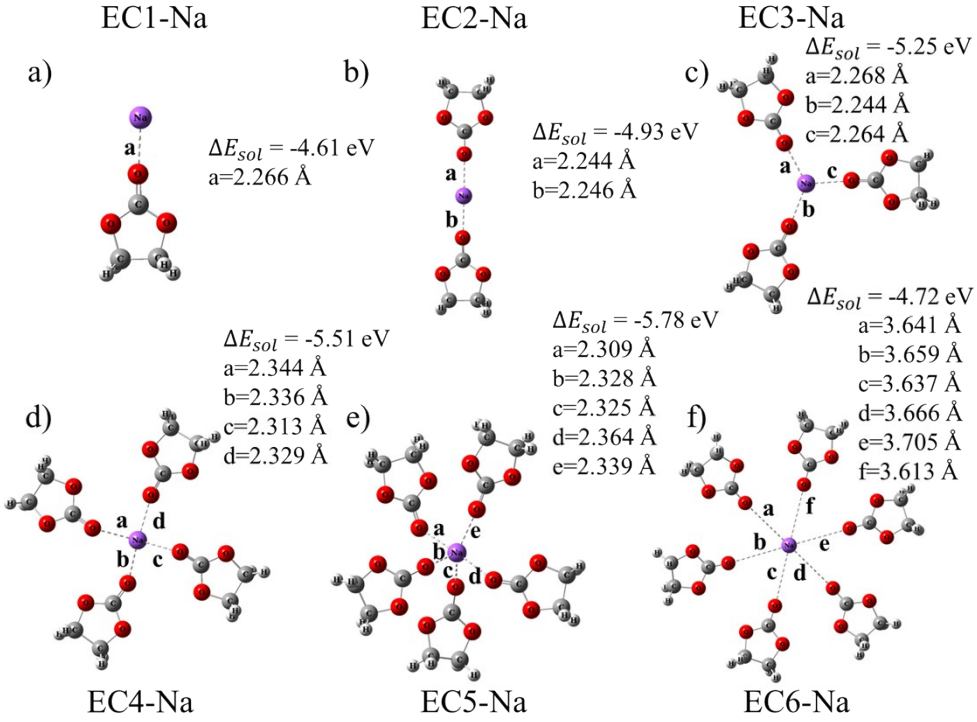

Figure S15. The optimized structures for a) EC1-Na, b) EC2-Na, c) EC3-Na, d) EC4-Na, e) EC5-Na and f) EC6-Na clusters.

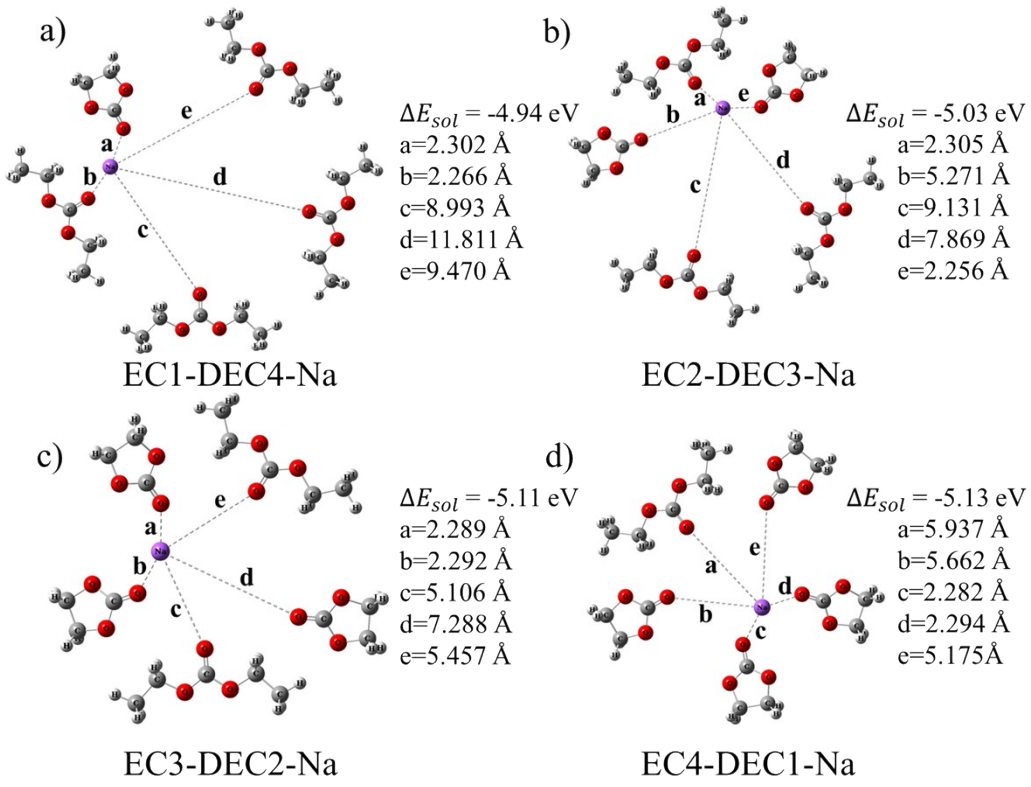

Figure S16. The optimized structures for a) EC1-DEC4-Na, b) EC2-DEC43-Na, c) EC3-DEC2-Na and d) EC4-DEC1-Na clusters.

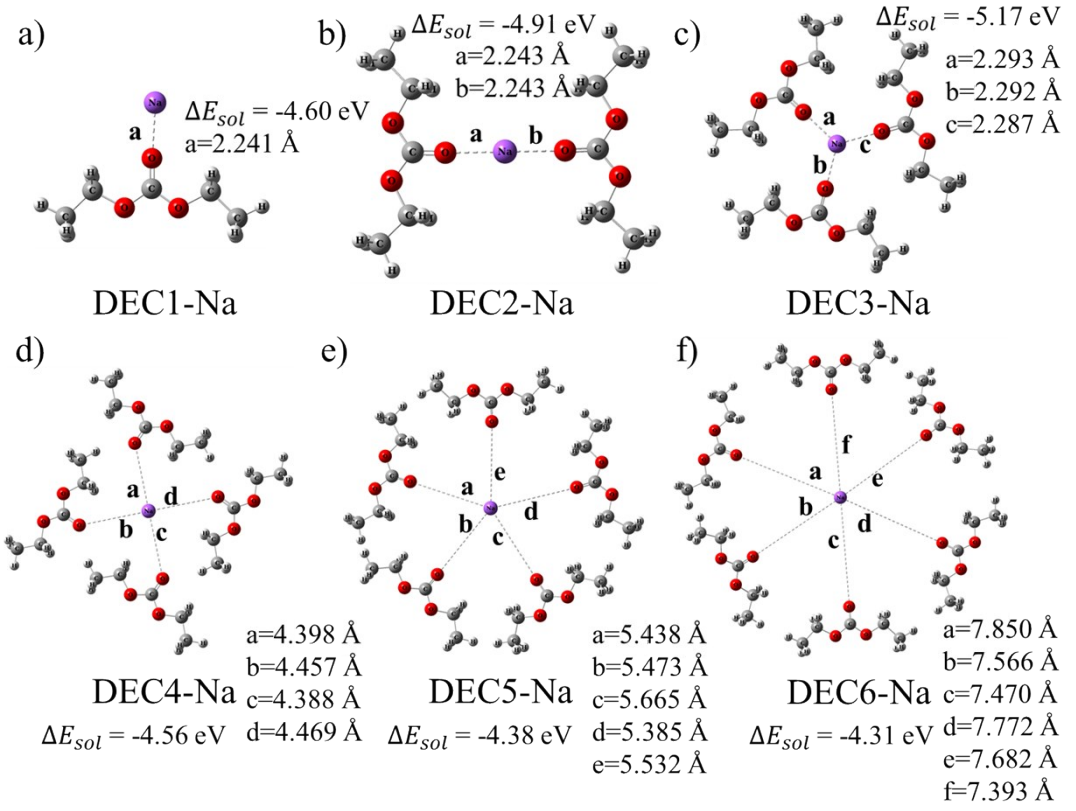

Figure S17. The optimized structures a) DEC1-Na, b) DEC2-Na, c) DEC3-Na, d) DEC4-Na, e) DEC5-Na and f) DEC6-Na clusters.

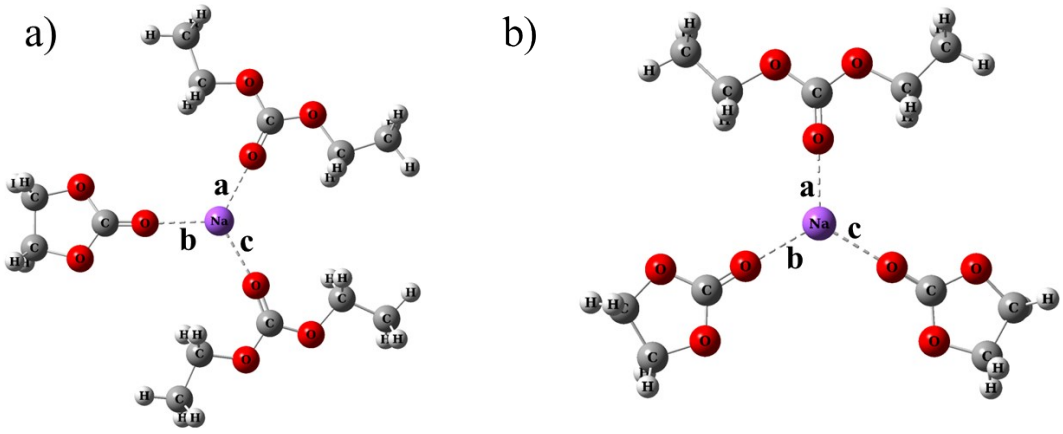

Figure S18. The optimized structures for a) DEC2-EC1-Na, and b) DEC1-EC2-Na clusters.

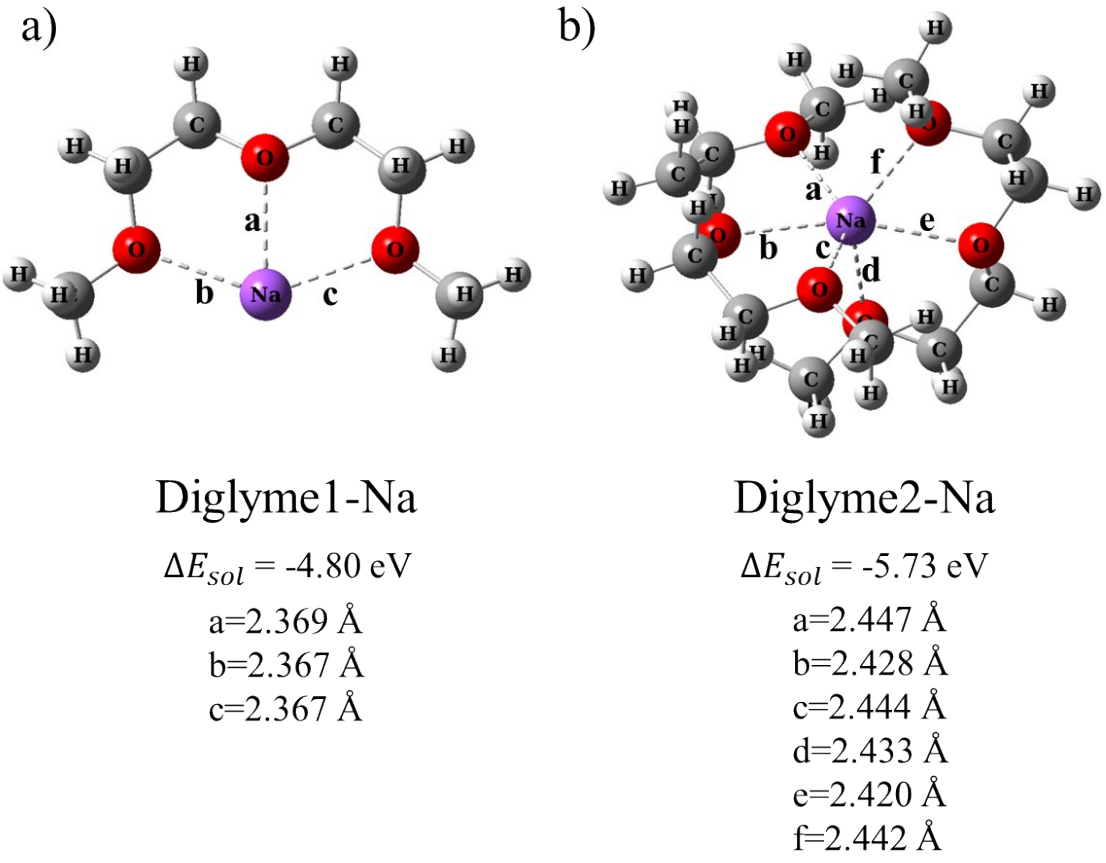

Figure S19. Optimized structures for a) diglyme1-Na, b) diglyme2-Na.

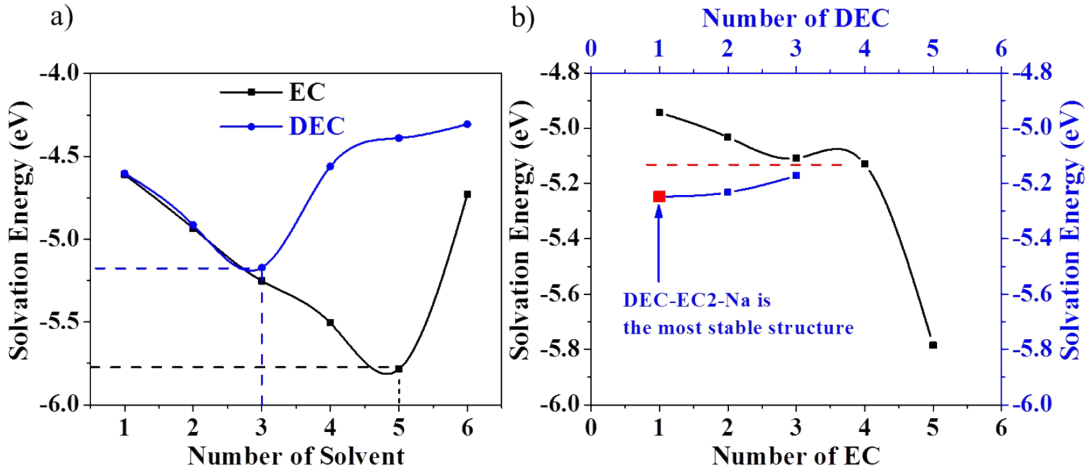

Figure S20. Calculated solvation energy of EC_x-Na (x=1, 2, 3, 4, 5, 6), DEC_x-Na (x=1, 2, 3, 4, 5, 6), $EC_xDEC_{5-x}Na$ (x=1, 2, 3, 4, 5) and $DEC_xEC_{3-x}Na$ (x=1, 2, 3).

For all cluster calculations, the solvation energy (ΔE_{sol}) was calculated using the following equation:

$$\Delta E_{sol} = E_{clusters} - E_{Na+} - E_{solvent} \quad \text{(S1)}$$

Where $E_{clusters}$, E_{Na+} and $E_{solvent}$ are the energies of solvent-Na clusters, Na^+ and solvent, respectively [7,8]. As shown in the optimized structures (Figure S15-S19), the clusters include EC1-Na, EC2-Na, EC3-Na, EC4-Na, EC5-Na, EC6-Na, EC1-DEC4-Na, EC2-DEC43-Na, EC3-DEC2-Na, EC4-DEC1-Na, DEC1-Na, DEC2-Na, DEC3-Na, DEC4-Na, DEC5-Na, DEC6-Na, DEC2-EC1-Na, DEC1-EC2-Na, diglyme1-Na, diglyme2-Na. The clusters of EC5-Na, DEC2-Na and DEC1-EC2-Na have similar geometrical configurations with the simulation results reported by Sankaranarayanan et al [7]. For the clusters of diglyme1-Na and diglyme2-Na, they also have similar bent structure with the complexes in previous work [9]. However, they also have slight distinctions of interatomic distances (about 10% averaged deviation with the reported work), which may be caused by different calculation software (SIESTA package) and functional (PerdewBurke-Ernzerhof for solid (PBEsol) + van der Waals (vdW) method). Moreover, the solvation energy in this work was calculated in the solvent reaction field with polarizable continuum model (PCM) [5], which was not included in the previous work.

From the solvation energy calculations (Figure S20a), the strongest ΔE_{sol} value for the interaction of Na^+ with different solvents in the clusters are seen for DEC_3Na and EC_5Na complexes, respectively. However, in the contrast experiments, the electrolytes comprise the solvents in the mixture of ethylene carbonate (EC) and diethyl carbonate (DEC) (volume ratio = 1:1), and thus, the clusters definitely comprise of the solvent molecule of EC and DEC simultaneously. Therefore, we further calculated the solvation energy of $DEC_xEC_{3-x}Na$ (x=1, 2, 3) and $EC_xDEC_{5-x}Na$ (x=1, 2, 3, 4, 5). As shown in Figure S20b, when the Na^+ is solvated by the binary mixtures of carbonate molecules (EC and DEC), the solvation energy values of $DEC_xEC_{3-x}Na$ are stronger than that of $EC_xDEC_{5-x}Na$. Although the solvation energy of EC_5Na is strongest among all of them, it does not involve the DEC molecule. As a result, we can obtain the most stable cluster of DEC-EC2-Na in the EC:DEC electrolyte with the strongest solvation energy value (-5.25 eV).

Regarding the configurations of diglyme in the electrolyte, it was mentioned in the previous works that diglyme molecules are in bent structure [9,10]. In view of diglyme1-Na, the Na ion interact with three ether oxygen (O) atoms from diglyme molecule. Furthermore, for $diglyme_2$-Na, two diglyme molecules rigidly coordinate to one Na ion surrounded by six ether O atoms, thus forming the highly stable configuration with two crossing diglyme molecules. Thus, we selected the diglyme molecule with bent structure as the input structure for calculations. After the calculation of solvation energy, it can be found that the cluster of diglyme2-Na (-5.73 eV) is more stable than diglyme1-Na (-4.80 eV), owing to the strong interaction among Na ion and six O atoms from two crossing bent diglyme molecules. In addition, it is stronger than that of DEC-EC_2-Na (-5.25 eV), suggesting stronger interaction between Na^+ and diglyme, and thus, impeding the desolvation of diglyme at the electrode surface and reducing

the possibility of side reaction (i.e., solvent decomposition) that occur at the electrode surface.

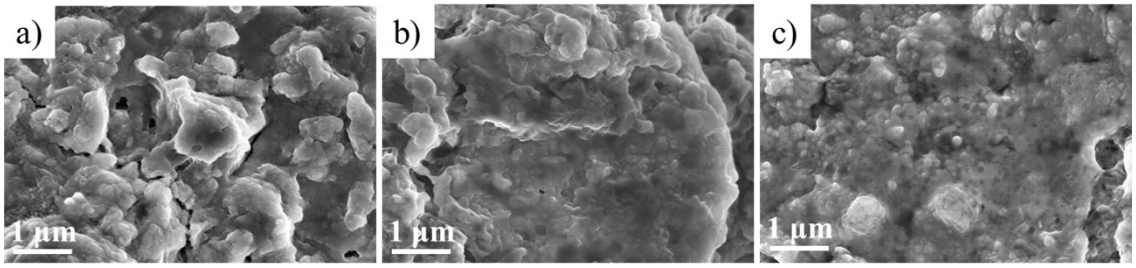

Figure S21. SEM images of the electrode surface after cycling at 100 mA g^{-1} for 1 cycle. a) cycled in the $NaCF_3SO_3$-diglyme electrolyte; b) cycled in the $NaClO_4$-EC: DEC electrolyte; c) cycled in the $NaPF_6$-EC: DEC electrolyte. To protect the electrode surface from contacting air, the cells were disassembled in an Ar-filled glove box filled and the electrodes were transferred to the SEM chamber using a sealed Ar-filled vessel.

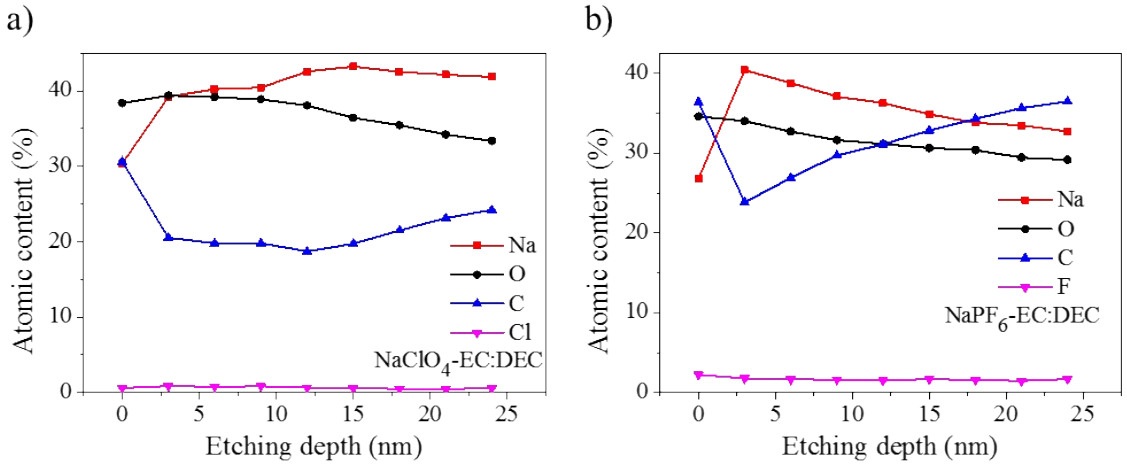

Figure S22. The atomic contents of various elements at different etching depth, calculated from the XPS depth profile, in the electrolyte of a) $NaClO_4$-EC: DEC and b) $NaPF_6$-EC: DEC electrolyte, respectively.

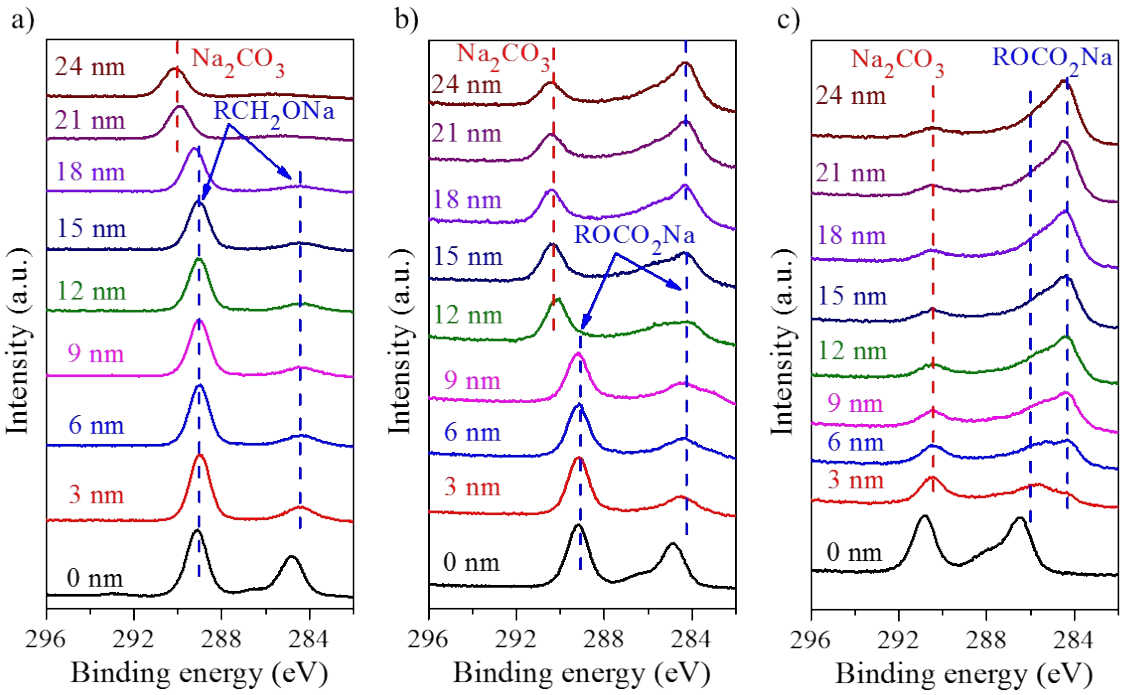

Figure S23. High-resolution XPS spectrums of C 1s at different etching depth. The electrode samples were collected in a) $NaCF_3SO_3$-diglyme electrolyte; b) $NaClO_4$-EC: DEC electrolyte; c) $NaPF_6$-EC: DEC electrolyte.

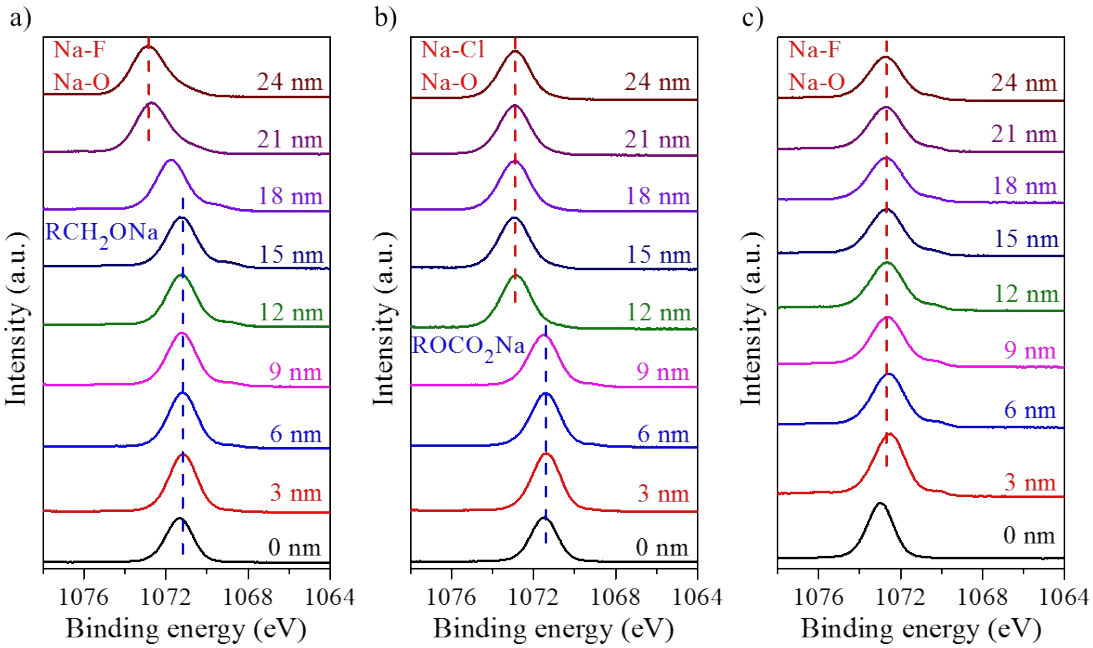

Figure S24. High-resolution XPS spectrums of Na 1s at different etching depth. The electrode samples were collected in a) $NaCF_3SO_3$-diglyme electrolyte; b) $NaClO_4$-EC: DEC electrolyte; c) $NaPF_6$-EC: DEC electrolyte.

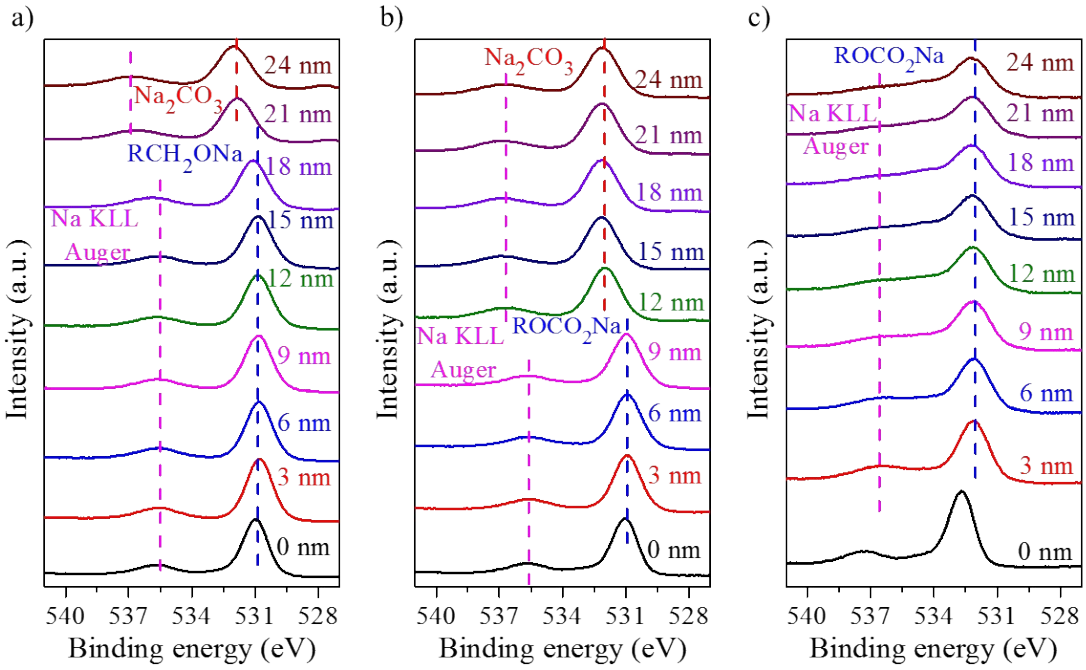

Figure S25. High-resolution XPS spectrums of O 1s at different etching depth. The electrode samples were collected in a) $NaCF_3SO_3$-diglyme electrolyte; b) $NaClO_4$-EC: DEC electrolyte; c) $NaPF_6$-EC: DEC electrolyte.

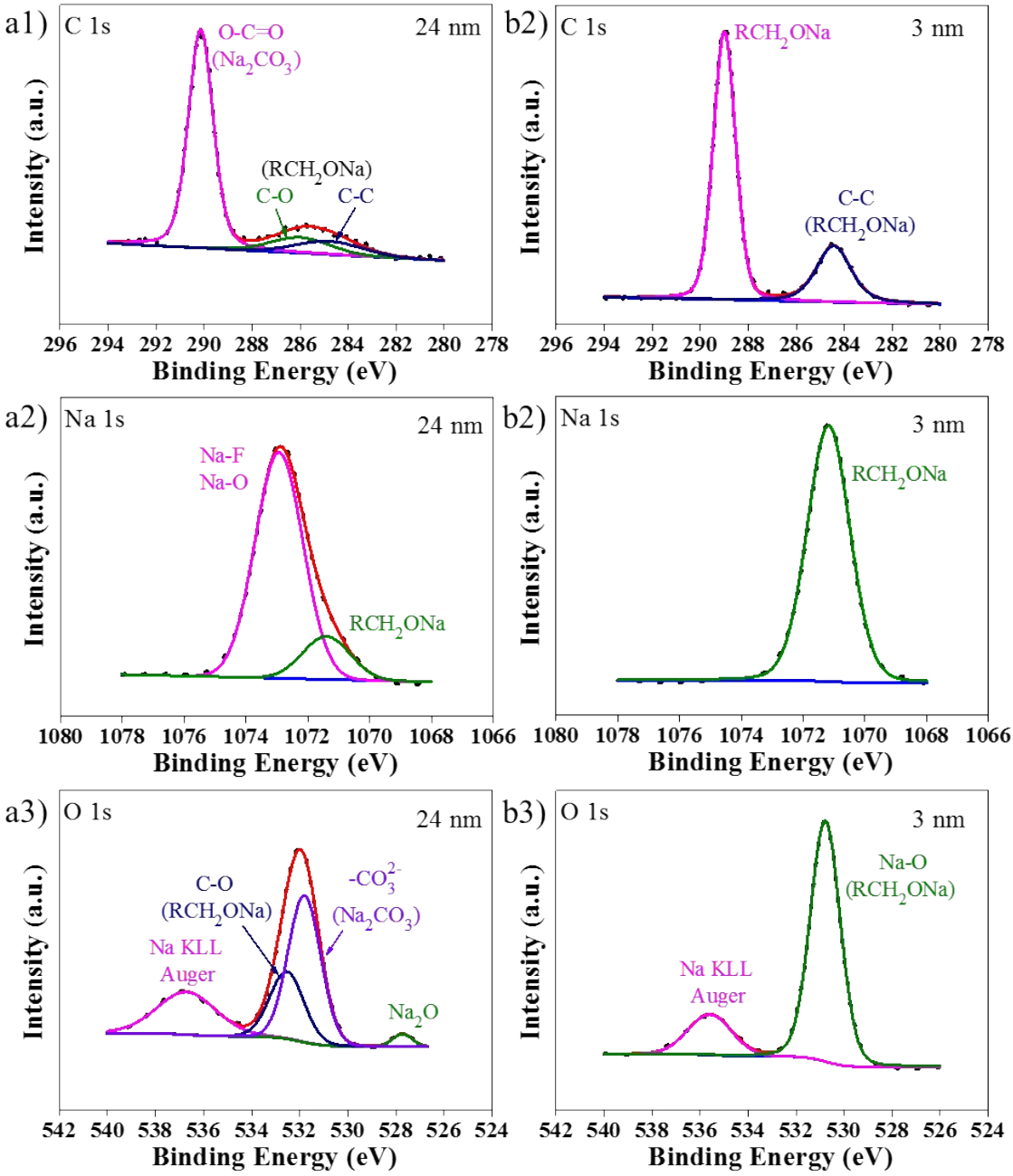

Figure S26. XPS C 1s, Na 1s and O 1s spectrums analysis at the etching depths of 3 and 24 nm in the $NaCF_3SO_3$-diglyme electrolyte.

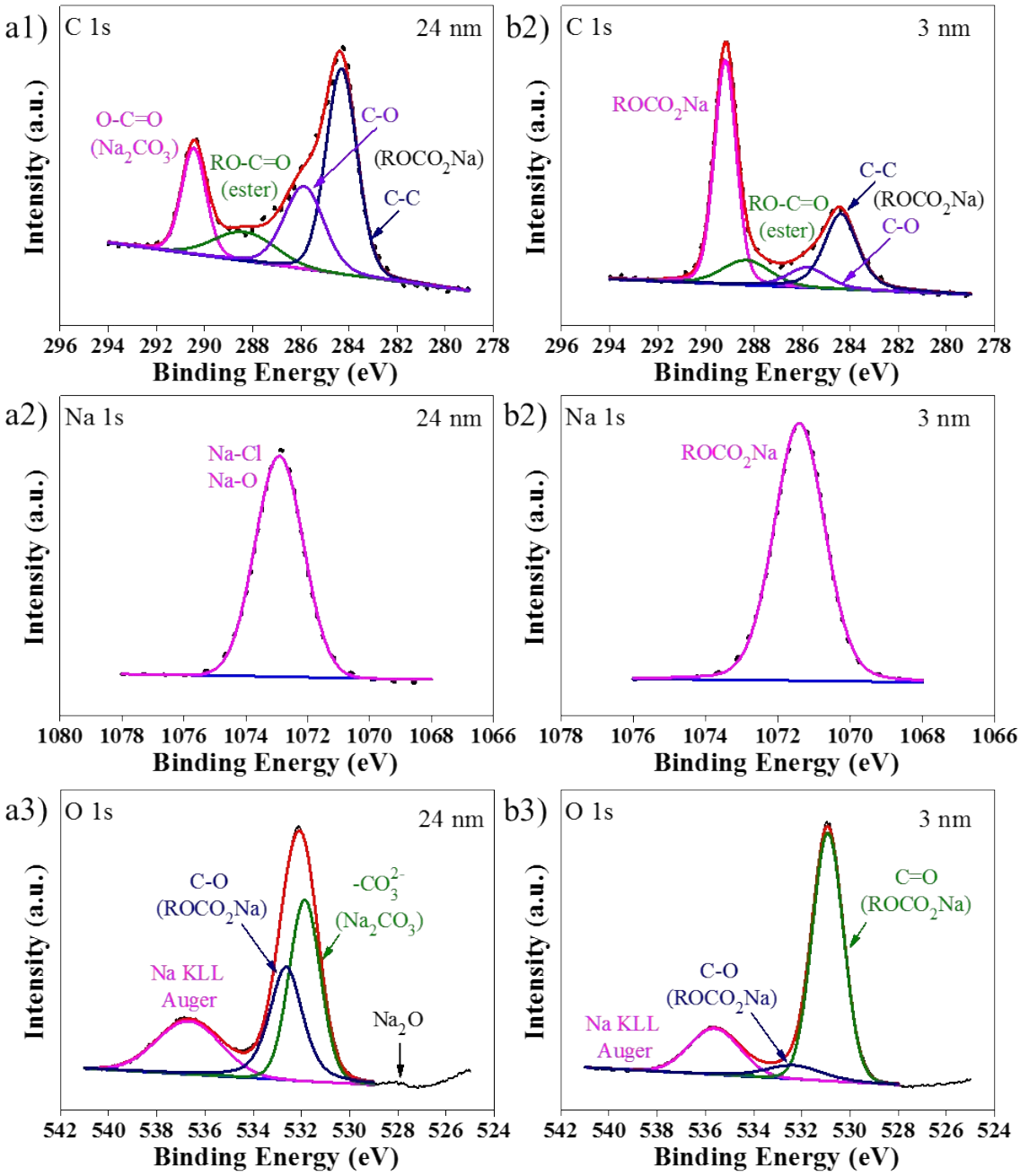

Figure S27. XPS C 1s, Na 1s and O 1s spectrums analysis at the etching depths of 3 and 24 nm in the $NaClO_4$-EC: DEC electrolyte.

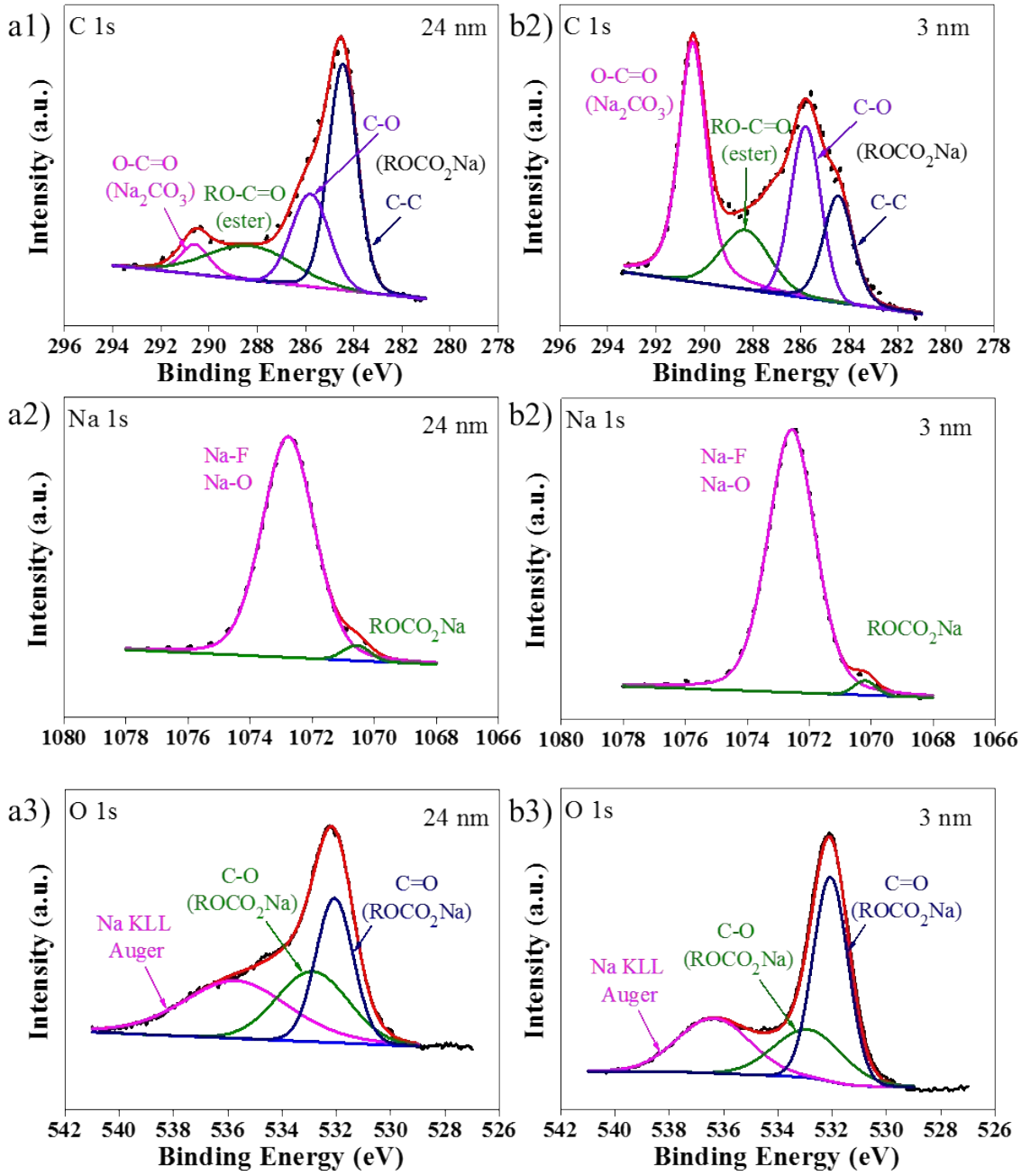

Figure S28. XPS C 1s, Na 1s and O 1s spectrums analysis at the etching depths of 3 and 24 nm in the $NaPF_6$-EC: DEC electrolyte.

Supplementary References

1 R. Blachnik and U. Wickel, *Z. Naturforsch*, 1982, **37b**, 1507–1513.

2 G. R. Burns, J. R. Rollo and J. D. Sarfati, *Inorganica Chim. Acta*, 1989, **161**, 35–38.

3 C. Lee, W. Yang and R. G. Parr, *Phys. Rev. B*, 1988, **37**, 785–789.

4 Gaussian 16, M. J. Frisch, G. W. Trucks, H. B. Schlegel, G. E. Scuseria, M. A. Robb, J. R. Cheeseman, G. Scalmani, V. Barone, G. A. Petersson, H. Nakatsuji, X. Li, M. Caricato, A. V. Marenich, J. Bloino, B. G. Janesko, R. Gomperts, B. Mennucci, H. P. Hratchian, J. V. Ortiz, A. F. Izmaylov, J. L. Sonnenberg, D. Williams-Young, F. Ding, F. Lipparini, F. Egidi, J. Goings, B. Peng, A. Petrone, T. Henderson, D. Ranasinghe, V. G. Zakrzewski, J. Gao, N. Rega, G. Zheng, W. Liang, M. Hada, M. Ehara, K. Toyota, R. Fukuda, J. Hasegawa, M. Ishida, T. Nakajima, Y. Honda, O. Kitao, H. Nakai, T. Vreven, K. Throssell, J. A. Montgomery, Jr., J. E. Peralta, F. Ogliaro, M. J. Bearpark, J. J. Heyd, E. N. Brothers, K. N. Kudin, V. N. Staroverov, T. A. Keith, R. Kobayashi, J. Normand, K. Raghavachari, A. P. Rendell, J. C. Burant, S. S. Iyengar, J. Tomasi, M. Cossi, J. M. Millam, M. Klene, C. Adamo, R. Cammi, J. W. Ochterski, R. L. Martin, K. Morokuma, O. Farkas, J. B. Foresman and D. J. Fox, *Gaussian, Inc., Wallingford CT, 2016*.

5 S. Miertuš, E. Scrocco and J. Tomasi, *Chem. Phys.*, 1981, **55**, 117–129.

6 A. D. Becke, *J. Chem. Phys.*, 1993, **98**, 5648–5652.

7 M. Shakourian-fard, G. Kamath, K. Smith, H. Xiong and S. K. R. S. Sankaranarayanan, *J. Phys. Chem. C*, 2015, **119**, 22747−22759.

8 T. A. Pham, K. E. Kweon, A. Samanta, V. Lordi and J. E. Pask, *J. Phys. Chem. C*, 2017, **121**, 21913–21920.

9 C. Yu, S. Ri, S. Choe, G. Ri, Y. Kye and S. Kim, *Electrochim. Acta*, 2017, **253**, 589–598.

10 A. C. S. Jensen, H. Au, S. Gärtner, M.-M. Titirici and A. J. Drew, *Batter. Supercaps*, 2020, **3**, 1306–1310.